Journal of Advanced Ceramics
2020, **9**(3): 292–302
https://doi.org/10.1007/s40145-020-0367-8
ISSN 2226-4108
CN 10-1154/TQ

Research Article

Energy storage properties of $0.87BaTiO_3$–$0.13Bi(Zn_{2/3}(Nb_{0.85}Ta_{0.15})_{1/3})O_3$ multilayer ceramic capacitors with thin dielectric layers

Hongxian WANG, Peiyao ZHAO, Lingling CHEN, Longtu LI, Xiaohui WANG*

State Key Lab of New Ceramic and Fine Processing, *School of Materials Science and Engineering*, *Tsinghua University*, *Beijing 100084*, *China*

Received: October 5, 2019; Revised: February 2, 2020; Accepted: February 12, 2020

Abstract: Multilayer ceramic capacitors (MLCCs) for energy storage applications require a large discharge energy density and high discharge/charge efficiency under high electric fields. Here, $0.87BaTiO_3$–$0.13Bi(Zn_{2/3}(Nb_{0.85}Ta_{0.15})_{1/3})O_3$ (BTBZNT) MLCCs with double active dielectric layers were fabricated, and the effects of inner electrode and sintering method on the energy storage properties of BTBZNT MLCCs were investigated. By using the pure Pt as inner electrode instead of $Ag_{0.6}Pd_{0.4}$ alloys, an alternating current (AC) breakdown strength (*BDS*) enhancement from 1047 to 1500 kV/cm was achieved. By investigating the leakage current behavior of BTBZNT MLCCs, the Pt inner electrode and two-step sintering method (TSS) were confirmed to enhance the Schottky barrier and minimize the leakage current density. With relatively high permittivity, dielectric sublinearity, and ultra-high *BDS*, the Pt TSS BTBZNT MLCCs exhibited a surprisingly discharge energy density (U_{dis}) of 14.08 J/cm^3. Moreover, under an operating electric field of 400 kV/cm, the MLCCs also exhibited thermal stability with U_{dis} variation < ±8% over a wide temperature (t) range from –50 to 175 ℃ and cycling reliability with U_{dis} reduction < 0.3% after 3000 charge–discharge cycles. These remarkable performances make Pt TSS BTBZNT MLCCs promising for energy storage applications.

Keywords: $BaTiO_3$; multilayer ceramic capacitor (MLCC); leakage current; energy storage

1 Introduction

Multilayer ceramic capacitors (MLCCs) have been widely investigated because of their high power density, fast charge–discharge capability, and long lifetime, compared with lithium-ion batteries, fuel cells, and electrochemical super capacitors [1–3]. They have potential applications in portable electronics, electric vehicles, medical devices, and pulsed power weapons; hence, low-cost and environmentally friendly MLCCs are urgently needed to fulfill these requirements [4,5]. Through the integration of multiple layers of ceramic capacitors, a large amount of energy can be stored and released by the MLCCs. The energy density (U) can be calculated by integrating the electric field (E) with the polarization (P) according to P–E hysteresis loops as shown in Eq. (1):

$$U = \int_0^P E\mathrm{d}P \tag{1}$$

Recently, $BaTiO_3$–$BiMeO_3$ (Me indicates the trivalent or meanly trivalent metallic cations) relaxor ferroelectrics have been of significant research interest [6–10]. Their markedly higher discharge/charge efficiency (E_{eff})

* Corresponding author.
E-mail: wxh@tsinghua.edu.cn

compared with ferroelectrics, allows for the realization of superior energy storage properties. In previous Ref. [11], $0.87BaTiO_3$–$0.13Bi(Zn_{2/3}(Nb_{0.85}Ta_{0.15})_{1/3})O_3$ MLCCs with dielectric thickness (D) of 4.8 μm were fabricated using the $Ag_{0.6}Pd_{0.4}$ (AgPd) inner electrode and two-step sintering method (TSS) [12]. The sub-micron grains (mean grain size, G = 434 nm) of $0.87BaTiO_3$–$0.13Bi$ $(Zn_{2/3}(Nb_{0.85}Ta_{0.15})_{1/3})O_3$ (BTBZNT) MLCCs are much smaller than the micron grains of reported ceramics for energy storage applications [13–21], and the dielectric layers therefore contained over 10 grains to obtain stable dielectric property. Because of their thin dielectric layers [22–28], remarkable AC breakdown strengthen (BDS) of 1047 kV/cm and a maximum discharge energy density (U_{max}) of 10.1 J/cm^3 were achieved.

Such MLCCs with thin dielectric layers are typically subjected to high AC operating electric fields to store and release a large amount of energy, and the possible thermal breakdown may occur when heat generated from the leakage current exceeds the heat lost [29]. The leakage current density (J) of the MLCCs is reported strongly dependent on the thermodynamic temperature (T) and electric field (E), and the Schottky emission model [30] is used to describe these leakage current behaviors, as shown in Eq. (2):

$$J = \left(\frac{4\pi e m^* k^2}{h^3}\right) T^2 \exp\left(\frac{-e\varphi_B + \sqrt{e^3 E / 4\pi\varepsilon_0\varepsilon_r}}{kT}\right) \quad (2)$$

where e is the effective electron mass, m^* is the effective Richardson constant, k is the Boltzmann constant, h is the Plank constant, φ_B is the Schottky barrier height, ε_0 is the vacuum permittivity, and ε_r is the relative permittivity at optical frequency. In an ideal Schottky barrier [31] (no electrode–dielectric interface states considered), the difference between the metal work function (φ_m, φ_{Pt} = 5.6 eV, φ_{Ni} = 5.1 eV [32], φ_{Pd} = 5.5 eV [33], m = Pt, Ni, Pd, etc.) and the semiconductor affinity (χ, χ_{BaTiO_3} = 3.9 eV) is the Schottky barrier height of the electrode–dielectric interface [34], as shown in Eq. (3):

$$\varphi_B = \varphi_m - \chi \quad (3)$$

However, the electrode–dielectric counter-diffusion is inevitable during the sintering process, and as-formed interfacial alloys [35–37] of minor work functions (φ_{Ba} = 2.7 eV, φ_{Ti} = 4.3 eV [31]) lower the Schottky barrier height. An effective approach to depress the formation of alloy is using a smart sintering method [38]. By increasing the heating rate from 200 to 3000 ℃/h, the interfacial alloy became thinner, and the Schottky barrier height was improved from 1.14 to 1.27 eV [39] in $BaTiO_3$ MLCCs. Therefore, this indicates that by using inner electrodes with large work function and a suitable sintering method, the Schottky barrier of MLCCs can be heightened, and thus, the leakage current density can be minimized.

In this study, BTBZNT MLCCs with thin dielectric layers using different inner electrodes and sintering methods were fabricated. The effects of inner electrode and sintering method on the energy storage property of BTBZNT MLCCs were investigated.

2 Material and methods

2. 1 Powder synthesizing

BTBZNT powders were synthesized via conventional solid-state reactions. Starting powders of $BaTiO_3$ (99.9% purity), Bi_2O_3 (analytical reagent, AR), ZnO (AR), Nb_2O_5 (99.99% purity), and Ta_2O_5 (99.9% purity, Ningxia Orient Tantalum Industry Co., Ltd., China) were first stoichiometrically weighed, and then ball-milled for 24 h in an isopropanol (AR) medium. The well-milled slurry was separated and dried at t = 80 ℃ for 12 h. The obtained powders were calcined at t = 900 ℃ for 4 h. All the powders except for Ta_2O_5, were purchased from Sinopharm Chemical Reagent Co., Ltd., China.

2. 2 MLCCs processing

The calcined powders were mixed in a solution with 27 wt% ethyl acetate (AR), 27 wt% ethyl alcohol (AR), and 1 wt% triglycerides as dispersant. The suspension solution was then ball-milled using zirconia balls for 24 h. The organics, including 10 wt% polyvinyl butyral (aerospace grade) as binder, 2 wt% polyethylene glycol (AR) and 2 wt% butyl benzyl phthalate (AR, Aladdin Biochemical Technology Co., Ltd., China) as plasticizer, were added, and the slurry was then ball-milled for an additional 24 h. All the organics except butyl benzyl phthalate were purchased from Sinopharm Chemical Reagent Co., Ltd., China. The well-milled slurry was separated and left to stand for 24 h to remove air. After roll-to-roll tape casting with a test coater (CMD-S1.7/D/4.OH/3-778, Yasui Seiki Corp, Japan), continuous tapes with thickness variation < ±0.2 μm

were formed. The Pt paste (MC-Pt100, GRIKIN Advanced Material Co., Ltd., China) was then screen printed on the green tapes with a size of 2.7 mm × 3.8 mm to serve as the inner electrode with an automated printing machine (NPM-1Y01, Yodogawa NCC Co., Ltd., Japan). Electrode patterned tapes were stacked with a 0.3 mm off-set from each other so that the effective electrode area was 2.7 mm × 3.2 mm. The active dielectric layer quantity and dielectric thickness were controlled using an automated laminating machine (NSM-1Y01, Yodogawa NCC Co., Ltd., Japan). After these processes, the BTBZNT MLCCs with double active dielectric layers ($D \approx 5$ μm) were fabricated via the two-step sintering method (TSS, held at t = 1185 ℃ for 1 min and then at t = 1015 ℃ for 3 h) or the one-step sintering method (OSS, held at t = 1115 ℃ for 2 h) in air.

2. 3 Characterization and testing method

The micro-structure was characterized via scanning electron microscopy (SEM; Supra 40/40vp, Carl Zeiss Corp, Germany) at an operating voltage of 15 kV and high-resolution transmission electron microscopy (HR-TEM; JEM-2010F, JEOL Ltd., Japan) at an operating voltage of 200 kV. The phase structures were detected via X-ray diffraction (XRD; D8 advance-A25, Bruker Co., Ltd., Germany). The temperature dependence of ε_r and dielectric loss (tanδ) were measured via an impedance analyzer (HP4278A; Hewlett-Packard, USA) with a temperature controller (Delta Design 9023, Cohu Semiconductor Equipment Group, USA). Hysteresis loops were measured using a ferroelectric measuring system (TF ANALYZER 2000E, aixACCT SystemsGmbH, Germany) at a frequency (f) of 10 Hz. The ε_r versus E curves were measured using a power device analyzer/curve tracer (Agilent B1505A; Agilent Technologies, USA) with an applied maximum direct current (DC) voltage (E = 400 kV/cm) and AC bias voltage (E = 10 kV/cm) at f = 10 Hz. The AC *BDS* at f = 10 Hz was measured using a high-voltage tester (YD2670B, Yangzi Electronic Co., Ltd., China). Unless specifically mentioned, all characterization and testing methods were carried out at room temperature (RT, t = 25 ℃).

3 Results and discussion

Figure 1 shows the micro-structure of the Pt BTBZNT MLCCs. The two-step sintering method [40], a universal method for preparing nanocrystalline ceramics, helped to decrease G of the Pt BTBZNT MLCCs from 346 to 271 nm.

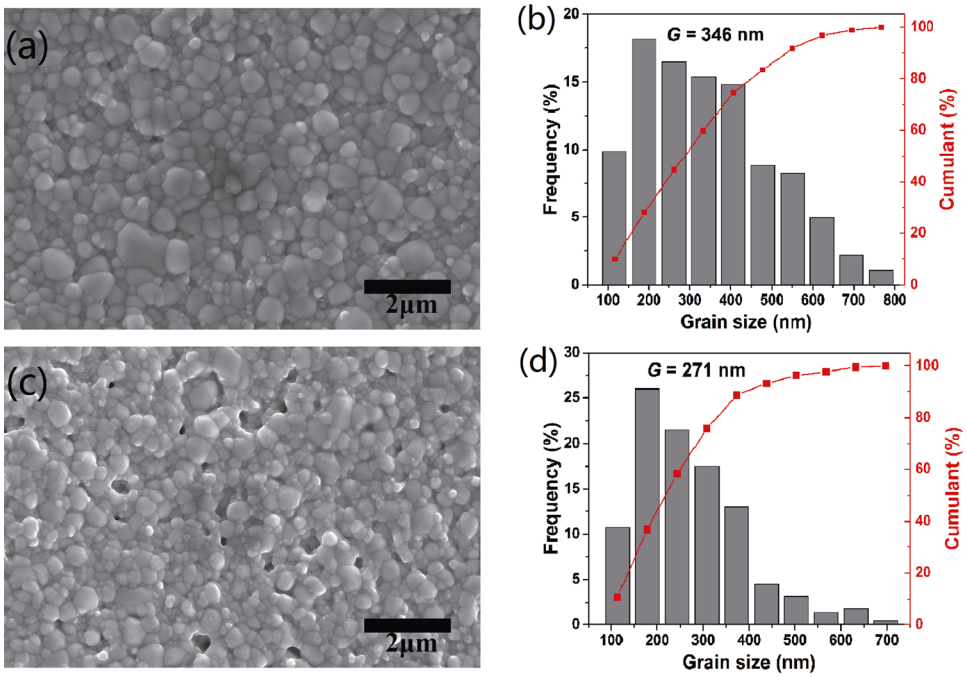

Fig. 1 SEM images of (a) Pt OSS and (c) Pt TSS BTBZNT MLCCs surface. Grain size distribution of (b) Pt OSS and (d) Pt TSS BTBZNT MLCCs.

Figure 2 shows the XRD patterns of the BTBZNT powders and Pt MLCCs. Perovskite phase structures with no split of the (002) and (200) peaks were detected, implying that all the dopants diffused into $BaTiO_3$ lattices forming a homogenous perovskite solid solution with symmetrical crystalline structure. The broader (002) peak of the Pt TSS MLCCs (full width at half maximum, $2\theta_{FWHM} = 0.142°$) than the Pt OSS MLCCs ($2\theta_{FWHM} = 0.104°$) implied finer grains according to Debye–Scherrer equation, which is consistent with SEM results.

Figure 3 shows the temperature dependence of the ε_r, dielectric loss, and temperature capacitance coefficients of the BTBZNT MLCCs. Because of the existence of PNRs in the grains [11], the BTBZNT MLCCs have a relatively high permittivity ($\varepsilon_r \approx 1200$) and a low dielectric loss ($\tan\delta < 0.5\%$ at $f = 100$ kHz) at RT. Broad Curie peaks can be observed in all MLCCs, and they arise from the random fields created by cation disorder because of the size and charge differences that disrupt the development of long-range polar ordering [41,42]. The Curie temperature (T_C) shifts to a higher value with increasing frequency, exhibiting the relaxor phenomenon with a strong diffuse phase transition [43]. The modified Curie–Weiss law [44] is used to describe the diffuse phase transition and is given by Eq. (4):

$$\frac{1}{\varepsilon_r} - \frac{1}{\varepsilon_m} = \frac{(t - t_m)^\gamma}{C'} \tag{4}$$

where ε_m is the maximum ε_r and t_m is t corresponding to ε_m. C' is the modified Curie–Weiss constant and γ is an indicator of the diffuseness degree. By changing the temperature dependence of ε_r at $f = 1$ kHz into the forms $\ln(1/\varepsilon - 1/\varepsilon_m)$ and $\ln(t - t_m)$, linear regressions

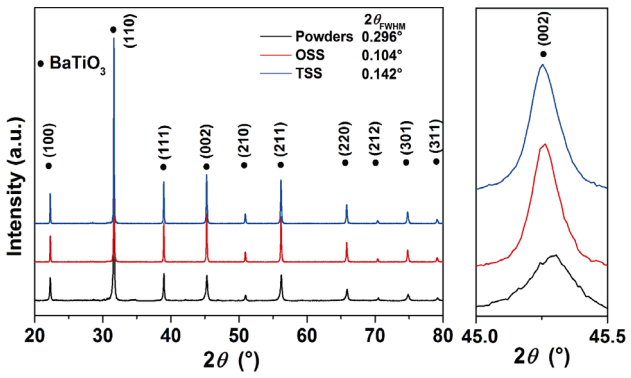

Fig. 2 XRD patterns of the BTBZNT powders and Pt BTBZNT MLCCs, and magnified patterns from 2θ = 45–45.5°.

with excellent correlations (goodness of fit, $R^2 > 0.999$) could be realized, as shown in Fig. 3 (insets). The large $\gamma > 1.7$ indicates the strong diffuse phase transition in the BTBZNT MLCCs. Because of the broad Curie peaks around RT, the temperature capacitance coefficients (TCCs) between 100 and 1 kHz are maintained at < ±15 % in the range of t = (–55) – 125 ℃, which meets the Electronics Industries Association (EIA) X7R specification.

The dielectric nonlinearity, which is the nonlinear reduction of the permittivity with increasing electric field, frequently degrades the energy storage properties of ceramics. The ε_r versus electric field and electric field capacitance coefficient (ECC) curves of the BTBZNT MLCCs are shown in Fig. 4. The gradual variation in ε_r with increasing E in the range of t = (–50) – 150 ℃ indicates the weak dielectric nonlinearity. The Johnson's phenomenological expression based on the Devonshire's phenomenological theory [45] is adopted to evaluate the dielectric nonlinearity, as shown in Eq. (5):

$$\frac{\varepsilon_r(E)}{\varepsilon_r(0)} = \frac{1}{(1 + \alpha\varepsilon_r(0)^3 E^2)^{1/3}} \tag{5}$$

where $\varepsilon_r(E)$ is the ε_r at E, $\varepsilon_r(0)$ is the ε_r at $E = 0$ kV/cm, and $\alpha\varepsilon_r(0)^3$ is an indicator of the degree of dielectric nonlinearity. By changing ε_r versus E curves into the forms $(\varepsilon_r(0)/\varepsilon_r(E))^3$ and E^2, linear regressions ($R^2 > 0.996$) were achieved, as shown in Fig. 4. The $\alpha\varepsilon_r(0)^3$ is one order lower than the $SrTiO_3$-surface-modified $BaTiO_3$ relaxor ferroelectrics ($\alpha\varepsilon_r(0)^3 \approx 9\times10^{-4}$) [46] with an approximate similar G, demonstrating the dielectric sublinearity of the BTBZNT MLCCs. Moreover, a further reduction in $\alpha\varepsilon_r(0)^3$ with increasing temperature significantly benefits the MLCC's high-temperature energy storage properties, as shown in Fig. 4 (insets).

Because all the MLCCs exhibited similar dielectric property, the effects of inner electrode and sintering method were negligible, considering of the uncertain effective electrode area and dielectric thickness after sintering. Figure 5 shows the complex impedance spectra and three series resistor–capacitance (3RC) equivalent circuit fitting of the BTBZNT MLCCs. By fitting the experimental data with 3RC equivalent circuit [47,48] as shown in Fig. 5, which were assigned to grain, grain-boundary, and electrode–dielectric interface. The Arrhenius relationship is adopted to evaluate the activation energy (E_a) of the insulation resistance (R_{ins}),

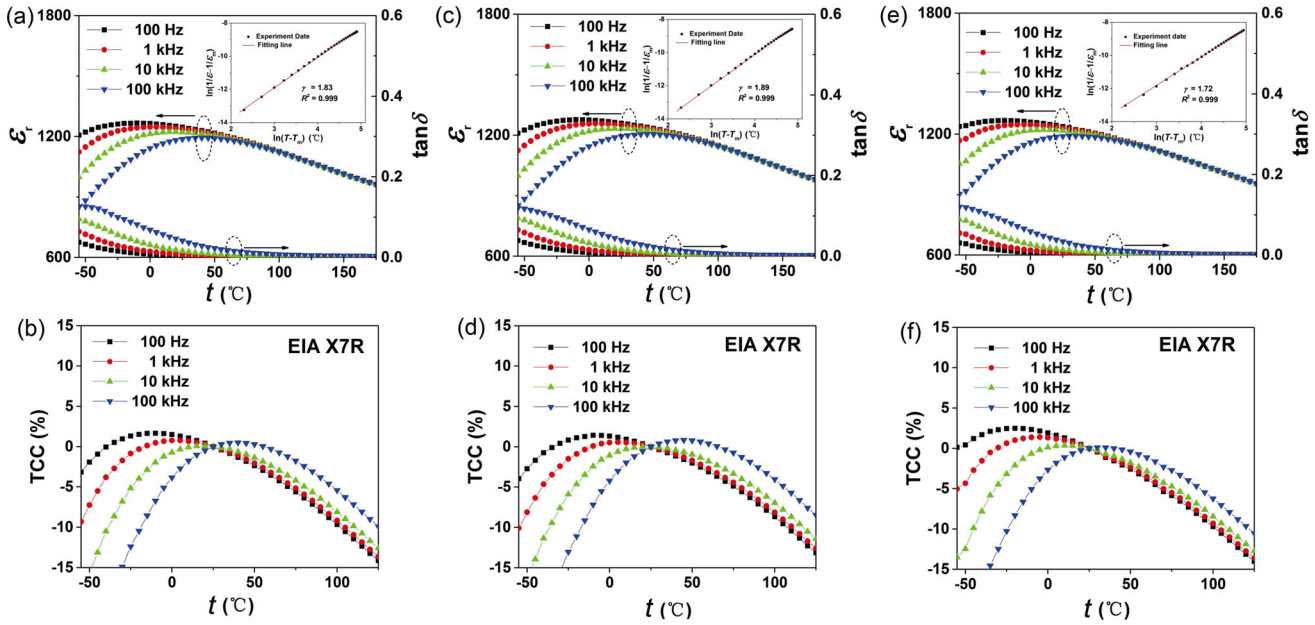

Fig. 3 Temperature dependence of the ε_r and dielectric loss of (a) Pt OSS, (c) Pt TSS, and (e) AgPd TSS BTBZNT MLCC. Insets are the modified Curies–Weiss law fitting. Temperature capacitance coefficient curves of (b) Pt OSS, (d) Pt TSS, and (f) AgPd TSS BTBZNT MLCC.

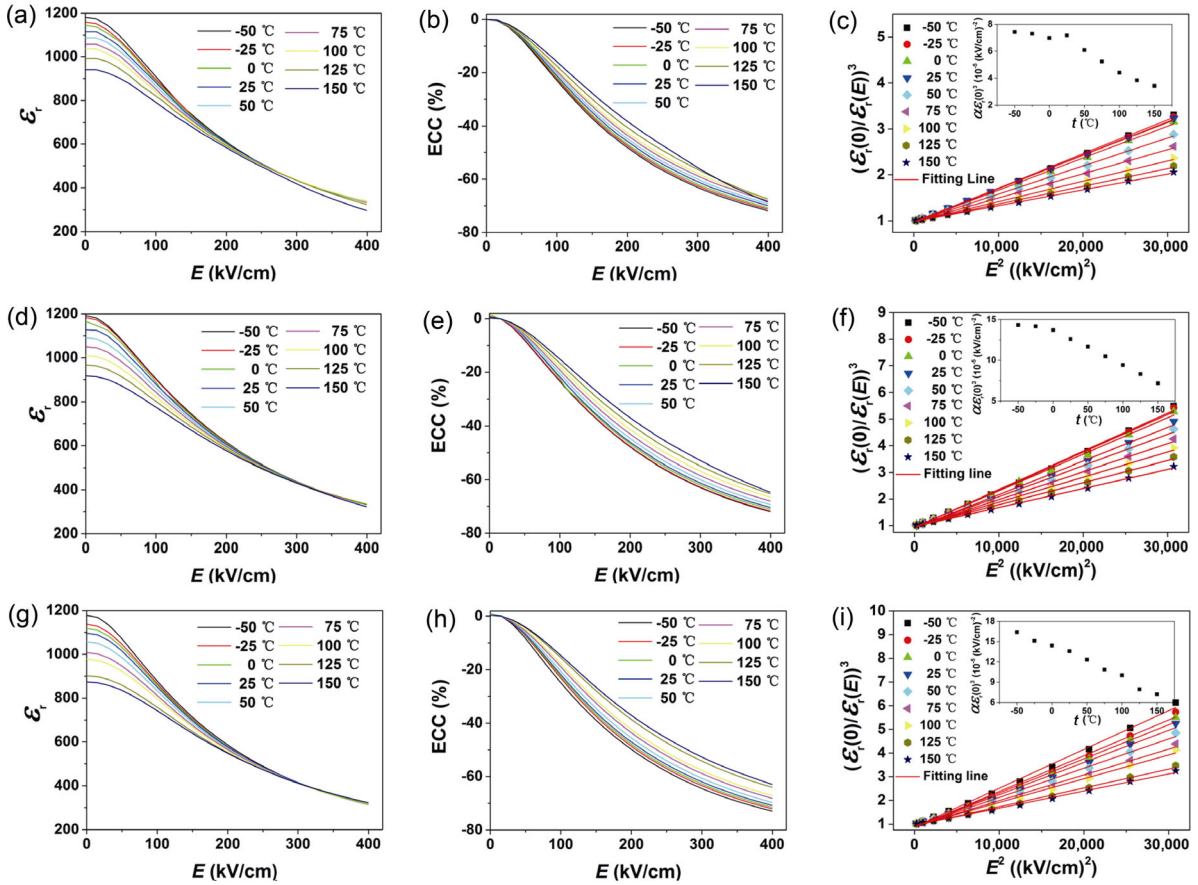

Fig. 4 ε_r versus the electric field curves of (a) Pt OSS, (d) Pt TSS, and (g) AgPd TSS BTBZNT MLCC. Electric field capacitance coefficient curves of (b) Pt OSS, (e) Pt TSS, and (h) AgPd TSS BTBZNT MLCC. (c) Johnson's phenomenological expression fitting of (g) Pt OSS, (h) Pt TSS, and (i) AgPd TSS BTBZNT MLCC. Insets show the temperature dependence of $\alpha\varepsilon_r(0)^3$.

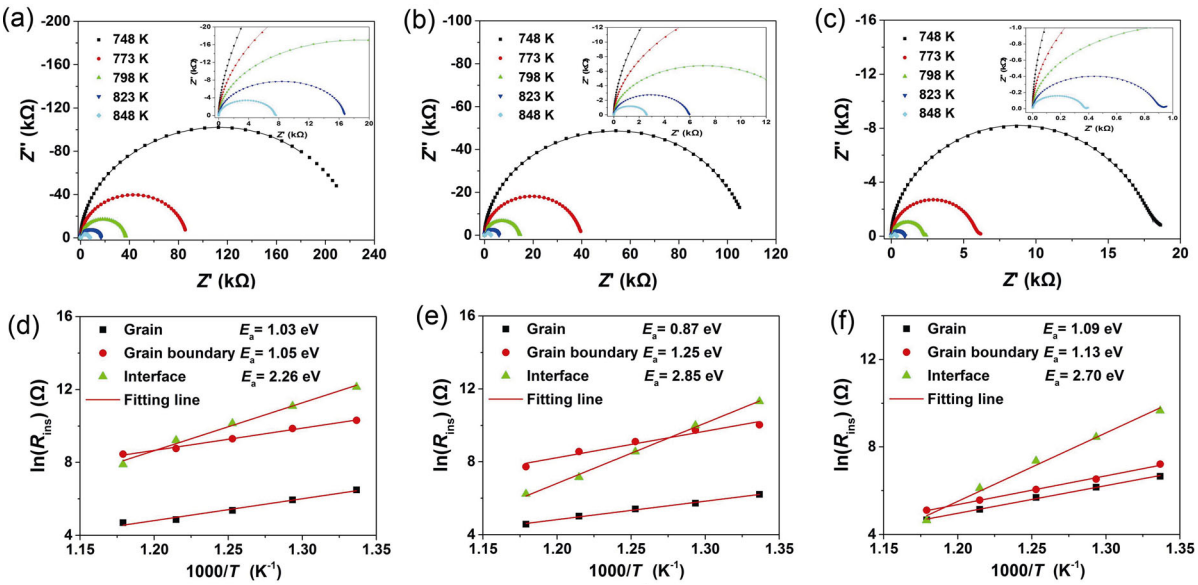

Fig. 5 Complex impedance spectra of experiment data and 3RC equivalent circuit fitting of (a) Pt OSS, (d) Pt TSS, and (g) AgPd TSS BTBZNT MLCC. Insets are magnified complex impedance spectra at higher temperatures. Arrhenius relationship fitting of the activation energy of (d) Pt OSS, (e) Pt TSS, and (f) AgPd TSS BTBZNT MLCC.

as shown in Eq. (6):

$$R_{\text{ins}} = R_0 \exp\left(\frac{E_a}{kT}\right) \tag{6}$$

where R_0 is the characteristic resistance. By changing the Arrhenius relationship into the forms ln(R_{ins}) and 1000/T as shown in Fig. 5. The E_a corresponding to the interface insulation resistance of the Pt TSS BTBZNT MLCC (E_a = 2.85 eV) was higher than that of the Pt OSS BTBZNT MLCC (E_a = 2.26 eV) and the AgPd TSS BTBZNT MLCC (E_a = 2.70 eV). The insulation resistance of grain (R_g), grain-boundary (R_{gb}), and interface (R_{int}) of the BTBZNT MLCCs at various temperatures are listed in Table 1.

To further investigate the conduction mechanisms, current–voltage measurements were performed. Figure 6 shows the leakage current curves and the Schottky thermionic emission model fitting of the BTBZNT MLCCs. Despite the approximate maximum leakage current density (J_{max} = 2.15 μA/cm^2) at T = 348 K, the higher J was detected for the AgPd TSS MLCC (J_{max} = 44.5 μA/cm^2) than the Pt OSS MLCC (J_{max} = 27.8 μA/cm^2) and the Pt TSS MLCC (J_{max} = 24.2 μA/cm^2) at T = 423 K, implying different φ_B according to Eq. (1). Leakage current data under E > 250 kV/cm were adopted and linear correlations of ln(J/T^2) and $E^{1/2}$ could be realized, guaranteeing the reliability of the Schottky thermionic emission model fitting results. The φ_B of the AgPd TSS, Pt OSS, and Pt TSS MLCC, evaluated from the plots of extrapolated values of ln(J/T^2) for $E \rightarrow 0$ versus 1000/T in Fig. 6 (insets), were 0.407, 0.431, and 0.489 eV, respectively.

The higher φ_B was obtained for the Pt TSS than AgPd TSS MLCC. It can be explained by the difference of the work function between Pt (φ_m = 5.6 eV) and $Ag_{0.6}Pd_{0.4}$ alloy (φ_m = 4.6 eV), which was evaluated by

Table 1 Comparison between the insulation resistances of the BTBZNT MLCCs

T (K)	Pt OSS			Pt TSS			AgPd TSS		
	R_g (Ω)	R_{gb} (Ω)	R_{int} (Ω)	R_g (Ω)	R_{gb} (Ω)	R_{int} (Ω)	R_g (Ω)	R_{gb} (Ω)	R_{int} (Ω)
748	663	29,939	186,620	498	22,506	81,645	780.4	1352	15,571
773	384	19,028	65,782	307	16,793	21,819	474.9	684.2	4678
798	215	10,987	25,487	225	8998	5156	297.1	425.6	1578
823	129	6378	10,076	151	5220	1271	173.2	262.5	452.1
848	109	4684	2663	97	2272	507	106.7	165	104

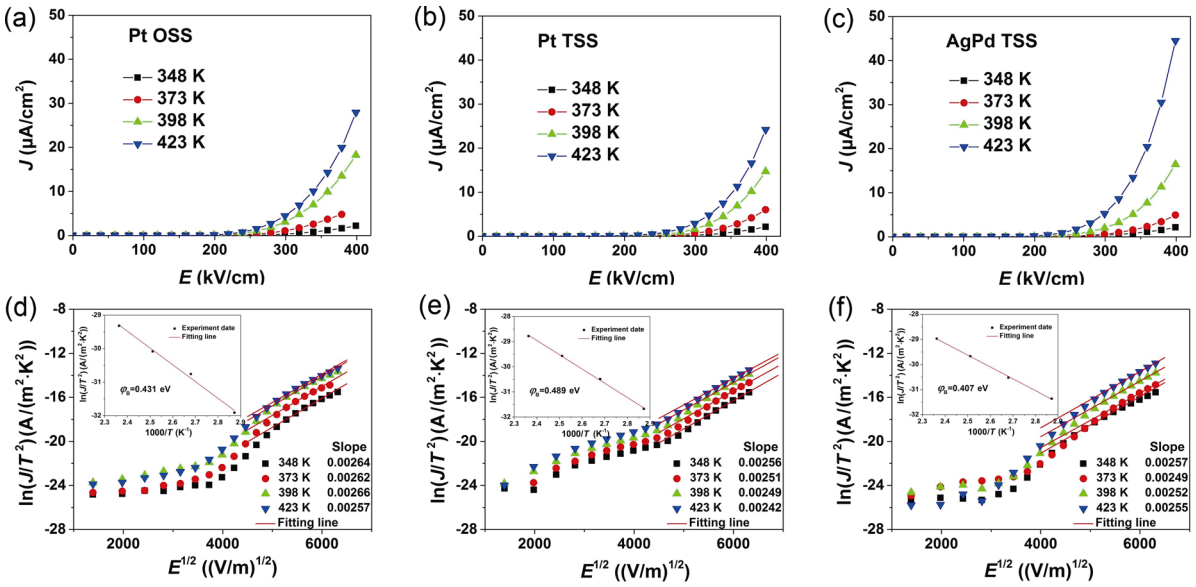

Fig. 6 Leakage current curves of (a) AgPd TSS, (b) Pt OSS and (c) Pt TSS BTBZNT MLCC. Schottky thermionic emission model fitting of (d) AgPd TSS, (e) Pt OSS, and (f) Pt TSS BTBZNT MLCC. Insets show the Schottky barrier height fitting.

the Freeouf empirical model [49] as given by Eq. (7):

$$\varphi^{\mathrm{Avg}} = \varphi_{\mathrm{M}}^{x}\varphi_{\mathrm{m}}^{1-x} \tag{7}$$

where φ_{M} and φ_{m} are the work functions of metal M and m, respectively, and x is the concentration of the metal. In addition, a higher φ_{B} was also obtained for the Pt TSS than Pt OSS MLCC, indicating that the two-step sintering method suppressed the formation of the interface (the thickness decreased from 35 to 30 nm as shown in Fig. 7), and thus heightened the Schottky barrier.

Figure 8 shows the hysteresis loops and the energy storage property of the BTBZNT MLCCs. The Pt TSS BTBZNT MLCC had an exceptional E_{max} = 1500 kV/cm, which was higher than the Pt OSS (E_{max} = 1301 kV/cm) and AgPd TSS (E_{max} = 1047 kV/cm) BTBZNT MLCC. Thus it was confirmed that using Pt and TSS were effective approaches minimizing the leakage current density, and thus enhancing the breakdown strengthen. The Weibull distribution was used to evaluate the AC

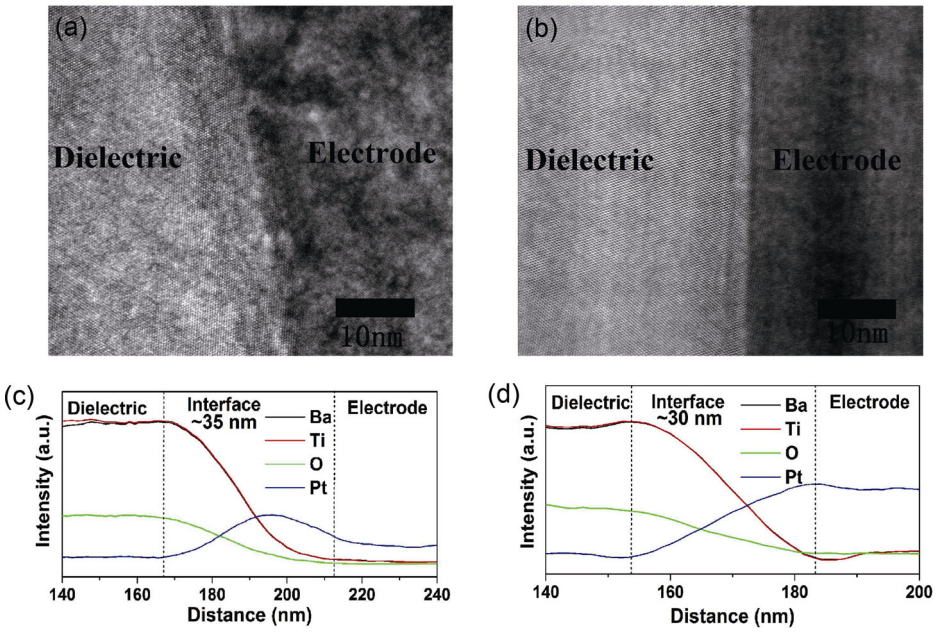

Fig. 7 TEM images of the electrode–dielectric interface of (a) Pt OSS and (b) Pt TSS BTBZNT MLCC. Elements line scanning of the electrode–dielectric interface of (c) Pt OSS and (d) Pt TSS BTBZNT MLCC.

BDS data, as given by Eq. (8):

$$P = 1 - \exp\left[-\left(\frac{E}{\alpha}\right)^{\beta}\right] \quad (8)$$

where P is the cumulative probability of failure, α is a scale parameter characterizing the breakdown strength, β is a shape parameter indicating the dispersion of the data, and E is the critical electric field above which breakdown occurs. The *BDS* data are ranked in ascending order and the values of P are estimated by Eq. (9):

$$P = \frac{i}{N+1} \quad (9)$$

where i is the rank and N is the total number of samples. α and β are then determined via linear regression of ln[–ln(1–P)] and ln$E$, as shown in Fig. 8(d) (inset). The large $\beta > 8$ guaranteed the reliability of the Weibull analysis, and α was in good agreement with the E_{max}. Despite of lowered E_{eff} under increasing E, the U_{dis} of the BTBZNT MLCC was compensated by the increasing maximum polarization, showing linear correlations of E and U_{dis} in Fig. 8(d). Because of the enhanced E_{max}, the U_{max} of the TSS BTBZNT MLCC was improved from 10.1 to 14.1 J/cm^3 using Pt instead of AgPd inner electrode.

The Pt TSS BTBZNT MLCC also had an excellent thermal stability and the cycling reliability of over 3000 charge–discharge cycles, as shown in Fig. 9, which were generally superior to the reported energy storage MLCCs [6,9,50–54], as listed in Table 2.

4 Conclusions

BTBZNT double-layer ceramic capacitors with $D \approx 5$ μm using the Pt or AgPd inner electrode were successfully fabricated via a one-step or two-step sintering method, and the Schottky thermionic emission was confirmed to dominate the conduction mechanism of the BTBZNT MLCCs. By investigating the leakage current behaviors of the BTBZNT MLCCs, using the Pt and TSS were proved to be effective approaches heightening φ_B, minimizing J, and thus enhancing *BDS*. The Pt TSS BTBZNT MLCC had the remarkable energy property with an E_{max} = 1500 kV/cm and a U_{max} = 14.1 J/cm^3, and an excellent thermal stability with variation < ±8% at t = (–50) – 150 ℃ and E = 400 kV/cm. The Pt TSS BTBZNT MLCC was generally superior than recently reported energy storage MLCCs, and the improvements in their electric properties further indicate that they have high potential for energy storage applications.

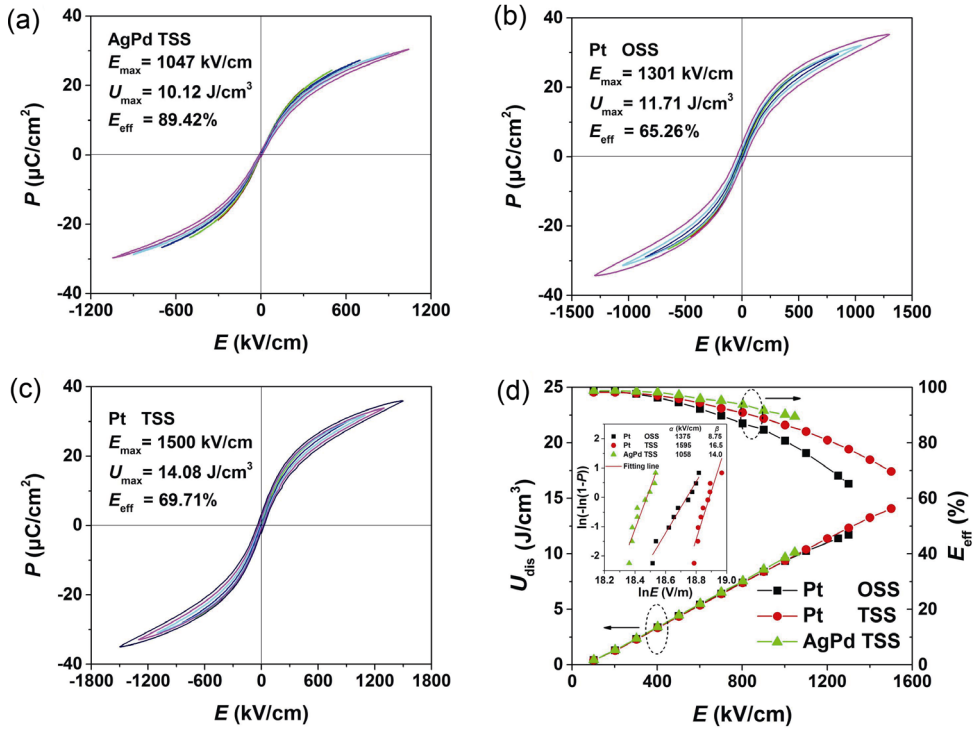

Fig. 8 Hysteresis loops of (a) AgPd TSS, (b) Pt OSS, and (c) Pt TSS BTBZNT MLCC. (d) Energy storage property of the BTBZNT MLCCs. Inset shows the Weibull distribution fitting results of AC *BDS*.

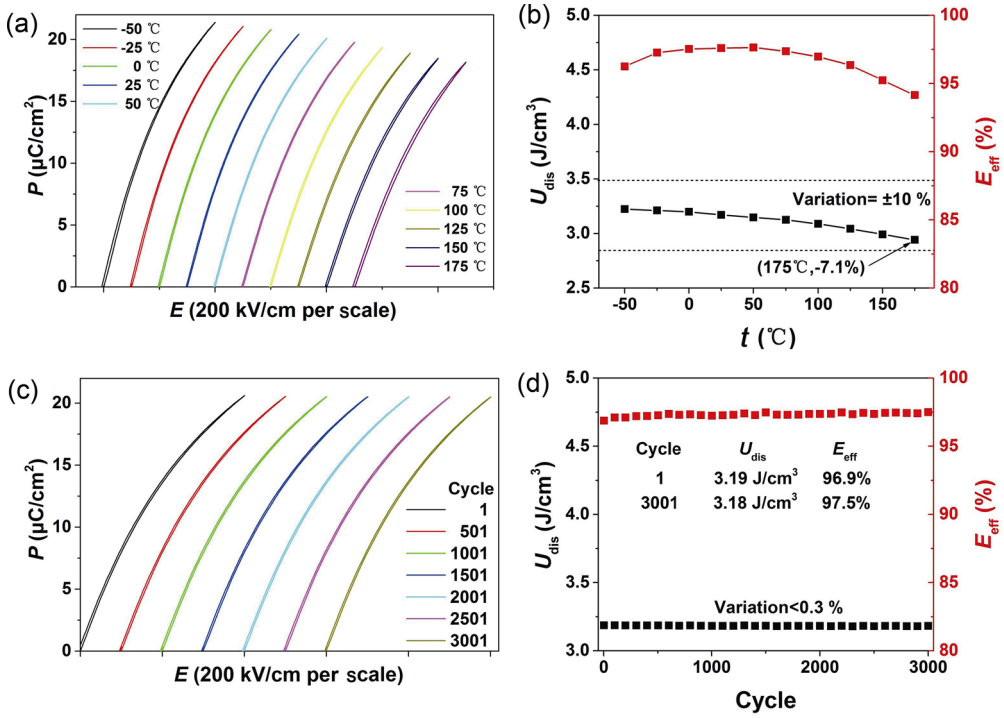

Fig. 9 (a) Hysteresis loop–temperature evolution. (b) Temperature dependence of the discharge energy density and discharge/charge efficiency. (c) Hysteresis loop–cycling evolution. (d) Cycling reliability of the discharge energy density and discharge/charge efficiency of the Pt TSS BTBZNT MLCC.

Table 2 Comparison between the energy storage property and the thermal stability of the reported MLCCs

MLCC	U_{max} (J/cm^3)	E_{max} (kV/cm)	E_{eff} (%)	Thermal stability of U_{dis}
This study	14.1	1500	69.7	Variation < ±8% at t = (–50) – 150 ℃ and E = 400 kV/cm
0.7BT–0.3BS [6]	6.1	730	—	—
0.8BT–0.2BZT [9]	2.8	330	—	—
0.62BF–0.3BT–0.08NZZ [50]	10.5	700	87	Variation < ±15% at t = 25 – 150 ℃ and E = 300 kV/cm
0.75BNF–0.25BT [51]	6.74	540	77	Variation < ±15% at t = 25 – 150 ℃ and E = 300 kV/cm
NBT–0.45SBT [52]	9.5	720	92	Variation < ±10% at t = (–60) – 120 ℃ and E = 350 kV/cm
0.9BT–0.1BLT [53]	4.05	466	95.5	—
PZST-based [54]	3.8	300	67.4	Variation < ±6% at t = 25 – 200 ℃ and E = 200 kV/cm

Acknowledgements

The study was supported by Ministry of Sciences and Technology of China through National Basic Research Program of China (973 Program 2015CB654604), National Natural Science Foundation of China for Creative Research Groups (Grant No. 51221291), National Natural Science Foundation of China (Grant No. 51272123), and CBMI Construction Co., Ltd.

References

[1] Liu C, Li F, Ma L P, *et al*. Advanced materials for energy storage. *Adv Mater* 2010, **22**: 28–62.

[2] Wu LW, Wang XH, Li LT. Lead-free $BaTiO_3$–$Bi(Zn_{2/3}Nb_{1/3})O_3$ weakly coupled relaxor ferroelectric materials for energy storage. *RSC Adv* 2016, **6**: 14273–14282.

[3] Shen ZB, Wang XH, Luo BC, *et al*. $BaTiO_3$–$BiYbO_3$ perovskite materials for energy storage applications. *J Mater Chem A* 2015, **3**: 18146–18153.

[4] Guo LM, Deng JN, Wang GZ, *et al*. N, P-doped CoS_2 embedded in TiO_2 nanoporous films for Zn-air batteries. *Adv Funct Mater* 2018, **28**: 1804540.

[5] Bi K, Bi MH, Hao YN, *et al*. Ultrafine core–shell $BaTiO_3$@SiO_2 structures for nanocomposite capacitors with high energy density. *Nano Energy* 2018, **51**: 513–523.

[6] Ogihara H, Randall CA, Trolier-Mckinstry S. Weakly coupled relaxor behavior of $BaTiO_3$–$BiScO_3$ ceramics. *J*

Am Ceram Soc 2009, **92**: 110–118.

[7] Choi DH, Baker A, Lanagan M, *et al*. Structural and dielectric properties in $(1–x)BaTiO_{3–x}Bi(Mg_1/_2Ti_1/_2)O_3$ ceramics ($0.1 \leqslant x \leqslant 0.5$) and potential for high-voltage multilayer capacitors. *J Am Ceram Soc* 2013, **96**: 2197–2202.

[8] Wang T, Jin L, Li CC, *et al*. Relaxor ferroelectric $BaTiO_3–Bi(Mg_{2/3}Nb_{1/3})O_3$ ceramics for energy storage application. *J Am Ceram Soc* 2015, **98**: 559–566.

[9] Kumar N, Ionin A, Ansell T, *et al*. Multilayer ceramic capacitors based on relaxor $BaTiO_3–Bi(Zn_{1/2}Ti_{1/2})O_3$ for temperature stable and high energy density capacitor applications. *Appl Phys Lett* 2015, **106**: 252901.

[10] Paterson A, Wong HT, Liu ZH, *et al*. Synthesis, structure and electric properties of a new lead-free ferroelectric solid solution of $(1−x)BaTiO_{3–x}Bi(Zn_{2/3}Nb_{1/3})O_3$. *Ceram Int* 2015, **41**: S57–S62.

[11] Zhao PY, Wang HX, Wu LW, *et al*. High-performance relaxor ferroelectric materials for energy storage applications. *Adv Energy Mater* 2019, **9**: 1803048.

[12] Chen I, Wang XH. Sintering dense nanocrystalline ceramics without final-stage grain growth. *Nature* 2000, **404**: 168–171.

[13] Li S, Nie HC, Wang GS, *et al*. Significantly enhanced energy storage performance of rare-earth-modified silver niobate lead-free antiferroelectric ceramics via local chemical pressure tailoring. *J Mater Chem C* 2019, **7**: 1551–1560.

[14] Tian Y, Jin L, Zhang HF, *et al*. High energy density in silver niobate ceramics. *J Mater Chem A* 2016, **4**: 17279–17287.

[15] Zhao L, Liu Q, Gao J, *et al*. Lead-free antiferroelectric silver niobate tantalate with high energy storage performance. *Adv Mater* 2017, **29**: 1701824.

[16] Qi H, Zuo RZ. Linear-like lead-free relaxor antiferroelectric $(Bi_{0.5}Na_{0.5})TiO_3–NaNbO_3$ with giant energy-storage density/efficiency and super stability against temperature and frequency. *J Mater Chem A* 2019, **7**: 3971–3978.

[17] Xu Q, Liu HX, Zhang L, *et al*. Structure and electrical properties of lead-free $Bi_{0.5}Na_{0.5}TiO_3$-based ceramics for energy-storage applications. *RSC Adv* 2016, **6**: 59280–59291.

[18] Li WB, Zhou D, Pang LX. Structure and energy storage properties of Mn-doped $(Ba,Sr)TiO_3–MgO$ composite ceramics. *J Mater Sci: Mater Electron* 2017, **28**: 8749–8754.

[19] Li WB, Zhou D, Pang LX, *et al*. Novel barium titanate based capacitors with high energy density and fast discharge performance. *J Mater Chem A* 2017, **5**: 19607–19612.

[20] Qu BY, Du HL, Yang ZT, *et al*. Enhanced dielectric breakdown strength and energy storage density in lead-free relaxor ferroelectric ceramics prepared using transition liquid phase sintering. *RSC Adv* 2016, **6**: 34381–34389.

[21] Shao TQ, Du HL, Ma H, *et al*. Potassium–sodium niobate based lead-free ceramics: Novel electrical energy storage materials. *J Mater Chem A* 2017, **5**: 554–563..

[22] Malec D, Bley V, Talbi F, *et al*. Contribution to the understanding of the relationship between mechanical and dielectric strengths of Alumina. *J Eur Ceram Soc* 2010, **30**: 3117–3123.

[23] Talbi F, Lalam F, Malec D. Dielectric breakdown characteristics of alumina. In Proceedings of 2010 10th IEEE International Conference on Solid Dielectrics, Potsdam, Germany, 2010: 1–4.

[24] Kim HK, Shi FG. Thickness dependent dielectric strength of a low-permittivity dielectric film. *IEEE Trans Dielect Electr Insul* 2001, **8**: 248–252.

[25] Chen HD, Udayakumar KR, Li KK, *et al*. Dielectric breakdown strength in sol–gel derived PZT thick films. *Integr Ferroelectr* 1997, **15**: 89–98.

[26] Chen G, Zhao JW, Li ST, *et al*. Origin of thickness dependent dc electrical breakdown in dielectrics. *Appl Phys Lett* 2012, **100**: 222904.

[27] Neusel C, Jelitto H, Schmidt D, *et al*. Thickness–dependence of the breakdown strength: Analysis of the dielectric and mechanical failure. *J Eur Ceram Soc* 2015, **35**: 113–123.

[28] Munz D, Fett T. Ceramics: mechanical properties, failure behaviour, materials selection. *Ann Chim-Sci Mat* 2000, **25**: 75.

[29] Zhang L, Hao H, Zhang SJ, *et al*. Defect structure-electrical property relationship in Mn-doped calcium strontium titanate dielectric ceramics. *J Am Ceram Soc* 2017, **100**: 4638–4648.

[30] Sze SM, Ng KK. *Physics of Semiconductor Devices*. 3rd edn. Hoboken, NJ, USA: John Wiley & Sons, Inc., 2007.

[31] Lüth H. *Scattering from Surfaces*. *Surfaces and Interfaces of Solids.* Berlin, Heidelberg: Springer Berlin Heidelberg, 1993: 136–217.

[32] Cann D, Maria JP, Randall CA. Relationship between wetting and electrical contact properties of pure metals and alloys on semiconducting barium titanate ceramics. *J Mater Sci* 2001, **36**: 4969–4976.

[33] Eastman DE. Photoelectric work functions of transition, rare-earth, and noble metals. *Phys Rev B* 1970, **2**: 1.

[34] Wang YP, Tseng TY. Electronic defect and trap-related current of $(Ba_{0.4}Sr_{0.6})TiO_3$ thin films. *J Appl Phys* 1997, **81**: 6762–6766.

[35] Yang GY, Dickey EC, Randall CA, *et al*. Oxygen nonstoichiometry and dielectric evolution of $BaTiO_3$. Part I—improvement of insulation resistance with reoxidation. *J Appl Phys* 2004, **96**: 7492–7499.

[36] Yang GY, Lian GD, Dickey EC, *et al*. Oxygen nonstoichiometry and dielectric evolution of $BaTiO_3$. Part II—insulation resistance degradation under applied dc bias. *J Appl Phys* 2004, **96**: 7500–7508.

[37] Yang GY, Lee SI, Liu ZJ, *et al*. Effect of local oxygen activity on Ni–$BaTiO_3$ interfacial reactions. *Acta Mater* 2006, **54**: 3513–3523.

[38] Polotai AV, Yang GY, Dickey EC, *et al*. Utilization of multiple-stage sintering to control Ni electrode continuity in ultrathin Ni–$BaTiO_3$ multilayer capacitors. *J Am Ceram*

Soc 2007**, 90**: 3811–3817.

[39] Polotai AV, Fujii I, Shay DP, *et al*. Effect of heating rates during sintering on the electrical properties of ultra-thin Ni–$BaTiO_3$ multilayer ceramic capacitors. *J Am Ceram Soc* 2008**, 91**: 2540–2544.

[40] Chen I, Wang XH. Sintering dense nanocrystalline ceramics without final-stage grain growth. *Nature* 2000, **404**: 168–171.

[41] Huang X, Hao H, Zhang S, *et al*. Structure and dielectric properties of $BaTiO_3$–$BiYO_3$ perovskite solid solutions. *J Am Ceram Soc* 2014, **97**: 1797–1801.

[42] Strathdee T, Luisman L, Feteira A, *et al*. Ferroelectric-to-relaxor crossover in $(1–x)BaTiO_{3–x}BiYbO_3$ ($0 \leqslant x \leqslant 0.08$) ceramics. *J Am Ceram Soc* 2011, **94**: 2292–2295.

[43] Nino JC, Lanagan MT, Randall CA, *et al*. Correlation between infrared phonon modes and dielectric relaxation in Bi_2O_3–ZnO–Nb_2O_5 cubic pyrochlore. *Appl Phys Lett* 2002, **81**: 4404–4406.

[44] Uchino K, Nomura S. Critical exponents of the dielectric constants in diffused-phase-transition crystals. *Ferroelectrics* 1982, **44**: 55–61.

[45] Xu Q, Zhang XF, Huang YH, *et al*. Effect of MgO on structure and nonlinear dielectric properties of $Ba_{0.6}Sr_{0.4}TiO_3$/MgO composite ceramics prepared from superfine powders. *J Alloys Compd* 2009, **488**: 448–453.

[46] Wu LW, Wang XH, Gong HL, *et al*. Core-satellite $BaTiO_3$@$SrTiO_3$ assemblies for a local compositionally graded relaxor ferroelectric capacitor with enhanced energy storage density and high energy efficiency. *J Mater Chem C* 2015, **3**: 750–758.

[47] Yang GY, Dickey EC, Randall CA, *et al*. Oxygen nonstoichiometry and dielectric evolution of $BaTiO_3$. Part I—improvement of insulation resistance with reoxidation. *J Appl Phys* 2004, **96**: 7492–7499.

[48] Yang GY, Lian GD, Dickey EC, *et al*. Oxygen nonstoichiometry and dielectric evolution of $BaTiO_3$. Part II—insulation resistance degradation under applied dc bias. *J Appl Phys* 2004, **96**: 7500–7508.

[49] Freeouf JL. Silicide Schottky barriers: An elemental description. *Solid State Commun* 1980, **33**: 1059–1061.

[50] Wang G, Li JL, Zhang X, *et al*. Ultrahigh energy storage density lead-free multilayers by controlled electrical homogeneity. *Energy Environ Sci* 2019, **12**: 582–588.

[51] Wang DW, Fan ZM, Zhou D, *et al*. Bismuth ferrite-based lead-free ceramics and multilayers with high recoverable energy density. *J Mater Chem A* 2018, **6**: 4133–4144.

[52] Li JL, Li F, Xu Z, *et al*. Multilayer lead-free ceramic capacitors with ultrahigh energy density and efficiency. *Adv Mater* 2018, **30**: 1802155.

[53] Li WB, Zhou D, Xu R, *et al*. $BaTiO_3$–$Bi(Li_{0.5}Ta_{0.5})O_3$, lead-free ceramics, and multilayers with high energy storage density and efficiency. *ACS Appl Energy Mater* 2018, **1**: 5016–5023.

[54] Chen LM, Sun NN, Li Y, *et al*. Multifunctional antiferroelectric MLCC with high-energy-storage properties and large field-induced strain. *J Am Ceram Soc* 2018, **101**: 2313–2320.